Impact of chemical reaction, thermal radiation and porosity on free convection Carreau fluid flow towards a stretching cylinder

Yeou Jiann Lim [a],[*], Sharidan Shafie [a],[*], Sharena Mohamad Isa [b],
Noraihan Afiqah Rawi [a], Ahmad Qushairi Mohamad [a]

[a] *Department of Mathematical Sciences, Faculty of Science, Universiti Teknologi Malaysia, 81310 Skudai, Johor Bahru, Johor, Malaysia*
[b] *Manufacturing Engineering Technology Section, Universiti Kuala Lumpur Malaysia Italy Design Institute (UniKL MIDI), Kuala Lumpur 56100, Malaysia*

Abstract Understanding fluid flow, heat, and mass transfer over a stretching cylinder is essential in ascertaining the quality of wire coating and coper thinning. This study looks at the influence of the heat source, thermal radiation, chemical reaction, and natural convection of Carreau fluid flows over a vertical stretching cylinder immersed in a porous medium. Suitable similarity variables are applied to convert the partial governing equations arising in fluid flows, heat, and mass transfer into ordinary differential equations. The optimal homotopy analysis method is then utilized to solve the transformed highly nonlinear governing equations. The impacts of the relevant parameters such as the Weissenberg number, porosity, heat source parameter, radiative number, chemical reaction parameter, mixed convection parameter, and curvature parameter on the dimensionless velocity, temperature, and concentration distribution as well as for the skin friction, Nusselt number, and Sherwood number are discussed through graphs and tables. It is observed that the velocity shows an opposite behavior as compared to temperature, and concentration in shear-thinning, $n < 1$, and shear-thickening, $n \geq 1$, fluid for an increment of the Weissenberg number. Additionally, the thickness of the momentum, thermal, and concentration boundary layer is enhanced by the curvature of the cylinder.

* Corresponding authors.
E-mail addresses: jiann@utm.my (Y.J. Lim), sharidan@utm.my (S. Shafie), sharena@unikl.edu.my (S.M. Isa), noraihanafiqah@utm.my (N.A. Rawi), ahmadqushairi@utm.my (A.Q. Mohamad).

1. Introduction

Fluid flows on a stretching cylinder are factors involved in many industrial manufacturing processes such as wire coating, coper thinning, paper production, photographic films, drawing

Nomenclature

Symbol	Description
c_p	specific heat ($\mathrm{J \cdot kg^{-1} \cdot K^{-1}}$)
C	concentration ($\mathrm{mol \cdot m^{-3}}$)
C_w	concentration at the wall ($\mathrm{mol \cdot m^{-3}}$)
C_∞	ambient concentration ($\mathrm{mol \cdot m^{-3}}$)
C_f	skin friction
$c_1, c_2, \cdots, c_7$	arbitrary constants
D	mass diffusivity ($\mathrm{m^2 \cdot s^{-1}}$)
f	dimensionless Stream function
f_0	initial guess of the dimensionless stream function
f_m	solution of m-order of the dimensionless stream function
g	gravity field ($\mathrm{m \cdot s^{-2}}$)
Gr	mixed convection parameter
K^*	permeability ($\mathrm{m^2}$)
K	porosity parameter
k^*	mean absorption coefficient ($\mathrm{m^{-1}}$)
l	characteristic length (m)
n	power-law index
Nu	Nusselt number
Pr	Prandtl number
p	embedding parameter
Q_0	heat source ($\mathrm{W \cdot m^{-3} \cdot K^{-1}}$)
Q	heat generation parameter
q_r	thermal radiation ($\mathrm{W \cdot m^{-2}}$)
Rd	radiation parameter
R^*	rate of chemical reaction ($\mathrm{s^{-1}}$)
R	radius of the cylinder (m)
Re_x	local Reynold number
Sh	Sherwood number
Sc	Schmidt number
T	temperature (K)
T_w	temperature at the wall (K)
T_∞	ambient temperature (K)
U_0	reference velocity ($\mathrm{m \cdot s^{-1}}$)
u	fluid velocity in the x- axis direction ($\mathrm{m \cdot s^{-1}}$)
v	fluid velocity in the r- axis direction ($\mathrm{m \cdot s^{-1}}$)
We	Weissenberg number

Greek symbols

α_∞	thermal conductivity away from the cylinder ($\mathrm{W \cdot m^{-1} \cdot K^{-1}}$)
$\alpha(T)$	temperature dependent thermal conductivity ($\mathrm{W \cdot m^{-1} \cdot K^{-1}}$)
β_T	volumetric coefficient of thermal expansion ($\mathrm{K^{-1}}$)
β	chemical reaction parameter
$\dot{\gamma}$	shear rate ($\mathrm{s^{-1}}$)
ε	small perturbation number
η	similarity variable
θ	dimensionless temperature
θ_0	initial guess of the dimensionless temperature
θ_m	solution of m- order of the dimensionless temperature
μ_0	zero-shear-rate viscosity ($\mathrm{kg \cdot m^{-1} \cdot s^{-1}}$)
μ_∞	infinite-shear-rate viscosity ($\mathrm{kg \cdot m^{-1} \cdot s^{-1}}$)
ρ	density ($\mathrm{kg \cdot m^{-3}}$)
σ^*	Stefan-Boltzmann constant ($\mathrm{W \cdot m^{-2} \cdot K^{-4}}$)
υ	kinematic viscosity ($\mathrm{m^2 \cdot s^{-1}}$)
ϕ	dimensionless concentration
ϕ_0	initial guess of the dimensionless concentration
ϕ_m	solution of m- order of the dimensionless concentration
ψ	stream function ($\mathrm{m^3 \cdot s^{-1}}$)
$\hbar_\theta$	non-zero control convergence parameters for the heat equation
$\hbar_\phi$	non-zero control convergence parameters for the concentration equation
$\hbar_f$	non-zero control convergence parameters for the momentum equation
λ	curvature parameter
Γ	relaxation time (s)

wire, metallurgy, hot rolling, and crude oil refinement. The quality of final products and the cost of manufacture are dependent on the rate of heat and mass transfer. Hence, the investigation of the boundary layer flow, heat transfer, and mass transfer along a stretching cylinder has gained considerable attention. The flow over a cylinder is normally considered as two-dimensional but when the radius of the cylinder has the same order as the boundary layer thickness, the flow may be acknowledged as axisymmetric. Therefore, a transverse curvature term is involved in the governing equations which have an essential impact on the velocity, concentration, and temperature profile. [1] studied the influence of the variable thermal conductivity and heat generation on the magnetohydrodynamic (MHD) flow and heat transfer over an impermeable horizontal stretching cylinder. Two types of heating processes namely prescribed surface temperature and prescribed heat flux were considered. The authors observed that the velocity profile and boundary layer thickness was enhanced by the curvature parameter.

[2] considered a steady mixed convection viscous flow and heat transfer toward a stretching cylinder under the effect of the thermal stratification. The obtained numerical results indicated that the local skin friction coefficient and the local Nusselt number were smaller for a flat plate as compared to a cylinder. [3] have numerically discussed the impact of the temperature jump on the laminar flow and heat transport through a stretching horizontal cylinder in the presence of a heat source with suction or injection and a magnetic field. They found that the fluid velocity and temperature far from the cylinder increased with the increase in the curvature parameter, but contradictory behavior was observed near the stretching surface. The effect of thermal radiation on the boundary layer viscous incompressible fluid flows through a stretching horizontal cylinder was reported by [4]. The impact of the various interesting parameters such as radiation parameter, temperature exponent parameter, Prandtl number, and curvature parameter on the velocity and temperature distribution had been analyzed.

A wide range of applications in engineering and geophysical fields such as ventilation procedure, geothermal, solar collectors, solid matrix heat exchanges, enhanced oil recovery, and cooling of nuclear reactors has made the study of convective fluid flow in a porous medium a great interest for research. [5] elucidated the problem of incompressible viscous fluid flows through a stretching horizontal cylinder embedded in a porous medium. The effect of the temperature jump was considered in the investigation. The authors observed that skin friction was a function of the permeability of the medium and the radius of the cylinder. Further, [6] examined the flow and thermal profiles of a mixed convection boundary layer flow in a porous medium towards a stretching vertical cylinder. The obtained numerical results by the study indicate that the porous parameter has increased the velocity profile but reduce the temperature distribution. [7] explored the distribution of the velocity and temperature in a viscous nanofluid flow over a stretching cylinder under the influence of free convection, viscous dissipation, heat sink, and thermal radiation in the existence of slip boundary conditions. The research found that the temperature profiles increased when a smaller natural convection parameter was applied. Additionally, the rate of the heat transfer was observed to be enhanced by reducing the porosity parameter.

Generally, the flow in nature has a diversity of characteristics. Several constitutive models have been derived to describe the rheological behavior of the fluid such as the Power-law fluid model, Ellis model, Casson fluid model, Herschel–Bulkley fluid model, Carreau fluid model, Bingham fluid model and cross fluid model [8]. The non-Newtonian fluid has been involved in many practical applications such as biological fluids, polymer processing, agricultural, petroleum, food productions, and chemical engineering. Regarding this, [9] have investigated the effect of thermal radiation, variable thermal conductivity, hall current, and porous medium on MHD Williamson fluid over a stretching cylinder in the presence of heat generation and ion slip. The consequence of various parameters such as Weissenberg number, curvature parameter, and thermal conductivity on the momentum and thermal boundary layer thickness were discussed. The Williamson fluid is a non-Newtonian fluid in which the viscosity of the fluid is dependent on the shear rate. [10] studied the free convection flow of the Casson fluid past an inclined stretching cylinder. The effects of the variable thermal conductivity, viscous dissipation, and thermal radiation were taken into account. The homotopy analysis method (HAM) was utilized to determine the analytical approximation solutions. The authors found that the curvature parameter, radiation parameter, and thermal conductivity parameter have enhanced the temperature profile.

The behavior of the tangent hyperbolic fluid over a stretching cylinder under the effect of a magnetic field and variable thermal conductivity was considered by [11]. The Keller-box method was used to compute the numerical solutions of the governing equations. The responses of the velocity and temperature to the various interesting parameters were displayed graphically and in tabulated form. [12] examined the character of a MHD Casson fluid flow, which was driven by a dissipated cylinder, under the influence of slip conditions and Newtonian heating. The numeric solutions of the governing equations were derived by utilizing the Runge-Kutta technique. More research on the non-Newtonian fluid and heat transfer over a stretching cylinder under different circumstances can be found in [13–19]. In addition, the importance of the mass transfer in fluid flows over a stretching cylinder has been emphasized by some researchers. [16] examined heat and mass transfer in MHD second-grade fluid near a stagnation point past a porous stretching cylinder. The effect of the temperature and concentration jump, Joule heating, and viscous dissipation on the velocity, temperature, and concentration profile has been discussed. The authors applied HAM to derive the series solutions of the resulting mathematical problems. The results indicated that the curvature parameter had increased the magnitude of the concentration profile.

[17] addressed the heat transfer and Williamson fluid flows over a stretching cylinder in the existence of homogeneous-heterogeneous reaction. An implicit finite difference method, namely the Keller-box technique was utilized to compute the solutions. The effects of several pertinent parameters such as curvature parameter, Weissenberg number, Pranthl number, and homogeneous and heterogeneous reaction on the velocity, temperature, and concentration profiles were analyzed. [18] considered the impact of the inclined magnetic field on a mixed convection second-grade fluid flow over a vertical stretching cylinder with Newtonian heating. Later, [19] deliberated a mathematical model to analyze the MHD Casson nanofluid flows toward an inclined stretching cylinder. The impacts of Casson parameter, curvature parameter, incline angle, natural convection, thermal radiation, Joule heating, viscous dissipation, heat generation, thermophoresis, and chemical reaction on the behavior of flow field profiles have been discussed and demonstrated graphically. HAM was applied to obtain the analytic approximations solutions for the highly nonlinear momentum equation, energy equation, and concentration equation respectively. The authors observed that the rate of mass transfer is enhanced by the curvature parameter, chemical reaction parameter, heat generation parameter, thermal radiation, and buoyancy parameters.

Recently, the Carreau fluid model, which had been derived by [20] to well overcome the shortcoming of the power-law fluid model, has attracted the attention of numerous researchers due to plenty of practical examples in chemical engineering, fiber technology, tinning of copper wire, and polymeric suspensions. The power-law fluid model fails to predict the viscosity of the fluid when the shear rate is too small or too large. [21] discussed the effect of the convective boundary conditions and Joule heating on the heat and mass transfer in Carreau nanofluid flow over an inclined stretching cylinder in the presence of a magnetic field. A numerical method namely the Runge-Kutta-Fehlberg method was used to solve the governing equations. The authors observed a reverse behavior for the velocity profile in shear-thickening fluids, while the velocity of the shear-thinning fluids was improved when a large value of the Weissenberg number was introduced. Further, [22] studied the unsteady heat and mass transfer of Carreau nanofluid flow, which was induced by an expanding or contracting horizontal cylinder, under the effect of convective surface conditions and temperature-dependent thermal conductivity. Also, the Brownian motion and thermophoresis were taken into consideration in the study. The numerical results of the problem were calculated by using the Matlab solver bvp4c.

[23] explored the influence of the nonlinear thermal radiation, Brownian motion, and thermophoresis on the unsteady stagnation point flow of MHD Carreau nanofluid along with an expanding cylinder. The characteristic of the velocity, temperature, and concentration distribution due to the various

embedded parameters was discussed by using the obtained numerical results computed by the Matlab solver bvp4c. The authors found that the temperature and concentration are lower when the cylinder was stretching instead of shrinking. [24] investigated the MHD boundary layer Carreau nanofluid flow over a horizontal extending cylinder by using Buongiorno's model. In the study, the effect of the generalized slip and chemical reaction was incorporated. The numerical solutions obtained by utilizing the Keller-box method have shown that the magnitude of the velocity and concentration was reduced by increasing the chemical reaction parameter.

The effect of the homogeneous-heterogeneous reactions on the MHD Carreau fluid flow over a stretching cylinder and the heat exchange process was elucidated by [25]. The resulting system of equations was determined by using the shooting method and was used to analyze the relationship between the embedded parameters and the velocity or temperature profile. [26] has recently studied Carreau nanofluid flow with thermally stratified and heat generation over a permeable cylinder in the presence of radiation and magnetic field. The shooting method was employed to compute the results of the similarity transformed governing equations. The results illustrated that the Sherwood number is larger in the presence of curvature compared to without curvature, and a similar phenomenon was observed for the skin friction. More interesting investigation about the Carreau fluid flows toward either a stretching cylinder or a stretching flat sheet can be found in [27–34].

From existing literature, the Carreau fluid flows with heat and mass transfer over a stretching vertical cylinder immersed in a porous medium under the effect of variable thermal conductivity, natural convection, thermal radiation, heat generation, and chemical reaction has not been investigated. The natural convection with thermal radiation is attracting a great attention on the tremendous applications in aerothermodynamics, nuclear reactor and climate change [35]. In a practical situation, the thermophysical properties such as thermal conductivity are deemed to be variable. For example,

the thermal conductivity of liquid metals is varied linearly with the temperature from 0 °F to 400 °F. In wake of the potential use in the manufacturing process and engineering industry, the present study aims to study the heat and mass transport in Carreau fluid flows through a stretching cylinder under the influence of buoyancy force, thermal radiation, heat generation, temperature-dependent thermal conductivity, porous medium and chemical reaction. HAM has been effectively used by researchers [10,16,19,36,37] to solve the fluid problem with different effects and physical geometry. The literature has shown that the method is efficient in dealing with highly nonlinear differential equations. Thus, this method is proposed in the present study for analyzing the behavior of the fluid field. Series solutions of the governing equations are calculated by using the HAM. The computational tasks in the present study are facilitated by using Mathematica solver BVPh2.0, which has been developed by the team of Shijun Liao [38–40].

2. Mathematical formulation

This investigation considers an incompressible Carreau fluid flow in a porous medium over a vertical stretching cylinder with the influence of free convection. The focus is on the effect of thermal radiation and heat generation on heat transfer in the fluid. Additionally, the mass transfer with the chemical reaction in the fluid is also analyzed. The fluid is assumed to be a steady two-dimensional axisymmetric boundary layer. As illustrated in Fig. 1, the x-axis is measured along the axis of the vertical cylinder and the r-axis is taken in the radial direction. The cylinder with radius R is stretched with a velocity $U_0 x/l$, where l is the characteristic length and U_0 is the reference velocity. The temperature and concentration at the surface of the cylinder are T_w and C_w respectively. The ambient fluid temperature is T_∞ ($T_w > T_\infty$) and concentration is C_∞ (see Fig. 1). The continuity, momentum, energy, and concentration equation in a vector notation are written as
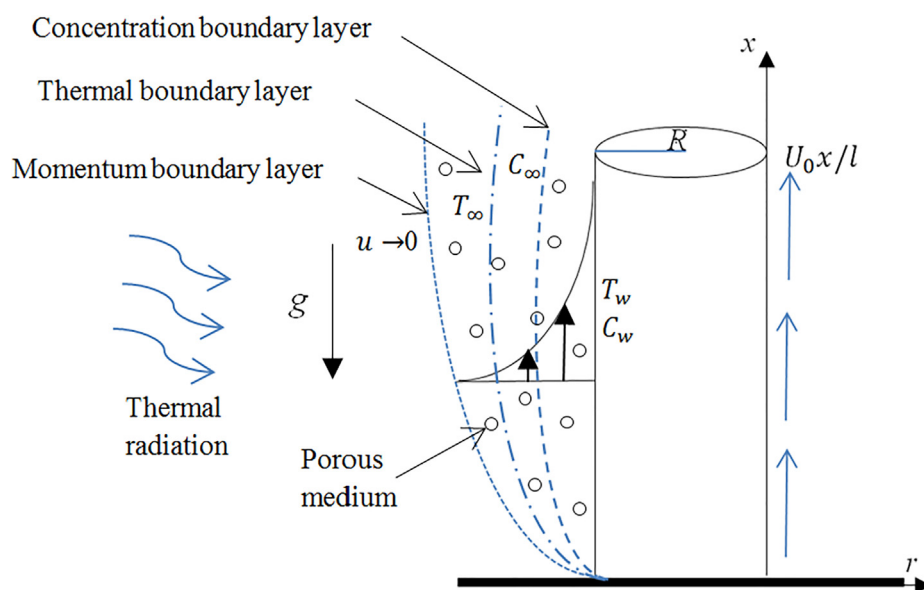
Fig. 1 Schematic geometry of the problem.

$$\nabla \cdot \mathbf{V} = 0, \tag{1}$$

$$(\mathbf{V} \cdot \nabla)\mathbf{V} = -\nabla p\mathbf{I} + \nabla \tau + \mathbf{F}, \tag{2}$$

$$\rho c_p (T \cdot \nabla)T = \nabla^2 [\alpha(T)T] + S_1, \tag{3}$$

$$(C \cdot \nabla)C = D\nabla^2 C + S_2, \tag{4}$$

where the velocity, energy and concentration are taken in form as $\mathbf{V} = (u(r,x), 0, v(r,x))$, $T = T(r,x)$ and $C = C(r,x)$ respectively. τ is the stress tensor, p is the pressure, $\mathbf{I}$ is the identity tensor, $\mathbf{F}$ is the volume force, S_1 is the external source/sink energy and S_2 is the external source/sink of the concentration.

Following [29,6], and [2], the Cauchy stress tensor for Carreau fluid is defined as

$$\tau = \mu \mathbf{A}_1, \tag{5}$$

and

$$\frac{\mu - \mu_\infty}{\mu_0 - \mu_\infty} = \left[1 + (\Gamma\dot{\gamma})^2\right]^{\frac{n-1}{2}}. \tag{6}$$

Where μ is the shear rate viscosity, $\mathbf{A}_1 = \nabla \cdot \mathbf{V} + (\nabla \cdot \mathbf{V})^T$ is the first kind Rivlin-Erickson tensor, μ_0 is the zero-shear-rate viscosity, μ_∞ is the infinite-shear-rate viscosity, Γ is a material time constant, and n is the power-law index. The shear rate is denoted by $\dot{\gamma}$ and is defined as

$$\dot{\gamma} = \sqrt{\frac{1}{2}\sum_i \sum_j \dot{\gamma}_{ij}\dot{\gamma}_{ij}} = \sqrt{\frac{1}{2}\prod} = \sqrt{\frac{1}{2}tr(A_1^2)}, \tag{7}$$

where $\prod$ is the second invariant strain tensor. The case for $\eta_\infty = 0$ and $\Gamma\dot{\gamma} < 1$ is considered, thus by binomial expansion, Eq. (6) can be represented as

$$\mu = \mu_0 \left[1 + \frac{n-1}{2}(\Gamma\dot{\gamma})^2\right]. \tag{8}$$

Eq. (5) can be rewritten as

$$\tau = \mu_0 \left[1 + \frac{n-1}{2}(\Gamma\dot{\gamma})^2\right] A_1, \tag{9}$$

by substituting μ in Eq. (5) by the μ in Eq. (8). The boundary layer approximation continuity and momentum equations for the free convection Carreau fluid towards a porous medium is obtained as

$$\frac{\partial(ru)}{\partial x} + \frac{\partial(rv)}{\partial r} = 0, \tag{10}$$

$$u\frac{\partial u}{\partial x} + v\frac{\partial u}{\partial r} = v\left(\frac{\partial^2 u}{\partial r^2} + \frac{1}{r}\frac{\partial u}{\partial r} + \frac{3\Gamma^2(n-1)}{2}\left(\frac{\partial u}{\partial r}\right)^2\frac{\partial^2 u}{\partial r^2} + \frac{\Gamma^2(n-1)}{2r}\left(\frac{\partial u}{\partial r}\right)^3\right) - \frac{v}{K^*}u + g\beta_T(T - T_\infty), \tag{11}$$

where g is the gravity field, β_T is the volumetric coefficient of thermal expansion, v is the kinematic viscosity, and K^* is the porosity. Eqs. (10) and (11) are subjected to non-slip boundary conditions

$$u = \frac{U_0 x}{l}, \quad v = 0, \quad at \quad r = R,$$
$$u \to 0, \quad as \quad r \to \infty. \tag{12}$$

Where x and r are the cylindrical polar coordinates taken in the axial and radial direction respectively.

In the existence of thermal radiation and heat generation, the boundary layer energy equation for the Carreau fluid through the stretching tube is governed by

$$u\frac{\partial T}{\partial x} + v\frac{\partial T}{\partial r} = \frac{1}{\rho c_p}\frac{1}{r}\frac{\partial}{\partial r}\left(\alpha(T)r\frac{\partial T}{\partial r}\right) - \frac{1}{\rho c_p}\frac{\partial q_r}{\partial r} + \frac{Q_0(T - T_\infty)}{\rho c_p}, \tag{13}$$

where q_r is the thermal radiation, Q_0 is the heat source, $\alpha(T)$ is the temperature-dependent thermal conductivity, c_p is specific heat and ρ is the density. The boundary conditions as following for Eq. (13) are

$$T = T_w, \quad at \quad r = R,$$
$$T \to T_\infty, \quad as \quad r \to \infty. \tag{14}$$

By using the Rosseland approximation, the derivative of the thermal radiation can be defined as

$$\frac{\partial q_r}{\partial r} = \frac{-16\sigma^* T_\infty^3}{3k^*}\frac{\partial^2 T}{\partial r^2}. \tag{15}$$

Where σ^* is the Stefan-Boltzmann constant and k^* is the mean absorption coefficient. Substitutes Eq. (15) into Eq. (13), we obtain

$$u\frac{\partial T}{\partial x} + v\frac{\partial T}{\partial r} = \frac{1}{r\rho c_p}\frac{\partial}{\partial r}\left(\alpha(T)r\frac{\partial T}{\partial r}\right) - \frac{1}{\rho c_p}\frac{-16\sigma^* T_\infty^3}{3k^*}\frac{\partial^2 T}{\partial r^2} + \frac{Q_0(T - T_\infty)}{\rho c_p}. \tag{16}$$

Within the range between 0°F and 400°F, the thermal conductivity of liquid metals is observed to be linearly proportional to the temperature. Thus, the thermal conductivity $\alpha(T)$ is a function of the temperature and can be taken as $\alpha(T) = \alpha_\infty(1 + \varepsilon\theta)$ [11,28]. α_∞ is the thermal conductivity at a large distance away from the cylinder and ε is the small number.

The boundary layer approximation diffusion corresponds to the concentration gradient in the Carreau fluid along with a stretching cylinder with the impact of a chemical reaction is modeled as

$$u\frac{\partial C}{\partial x} + v\frac{\partial C}{\partial r} = D\frac{1}{r}\frac{\partial}{\partial r}\left(r\frac{\partial C}{\partial r}\right) - R^*(C - C_\infty). \tag{17}$$

Where C is the concentration, R^* is the rate of chemical reaction and D is the mass diffusivity. Similar boundary conditions as shown in Eq. (14) are conducted for the concentration distribution. It is defined as

$$C = C_w, \quad at \quad r = R,$$
$$C \to C_\infty, \quad as \quad r \to \infty. \tag{18}$$

The following similarity variables are introduced to reduce the partial differential Eqs. (10)–(11), (16), and (17) into ordinary differential equations.

$$\eta = \sqrt{\frac{U_0}{vl}}\left(\frac{r^2 - R^2}{2R}\right), \quad \theta = \frac{T - T_w}{T_w - T_\infty},$$
$$\phi = \frac{C - C_w}{C_w - C_\infty}, \quad \psi = \sqrt{\frac{vU_0}{l}}xRf(\eta). \tag{19}$$

Substitute Eq. (19) into Eqs. (10), (11), (16) and (17). Eq. (10) or the continuity equations is automatically satisfied and Eqs. (11), (16), and (17) are simplified into

$$\frac{3(n-1)}{2}We^2(1+2\lambda\eta)(f'')^2(\lambda f'' + (1+2\lambda\eta)f''') + 2\lambda f'' + Gr\theta +$$
$$(1+2\lambda\eta)f''' + \frac{(n-1)}{2}We^2\lambda(1+2\lambda\eta)(f'')^3 + ff'' - (f')^2 - Kf' = 0,$$
(20)

$$(1+2\lambda\eta)(1+\varepsilon\theta+\frac{4}{3}Rd)\theta'' + (1+2\lambda\eta)(\theta')^2\varepsilon +$$
$$\Pr Q\theta + \left(2\lambda + \Pr f + 2\lambda\varepsilon\theta + \frac{4}{3}\lambda Rd\right)\theta' = 0,$$
(21)

$$(1+2\lambda\eta)\phi'' + (2\lambda + Scf)\phi' - Sc\beta\phi = 0,$$
(22)

with boundary conditions

$$f(0) = 0, \quad f'(0) = 1, \quad f'(\infty) = 0,$$
$$\theta(0) = 1, \quad \theta(\infty) = 0,$$
$$\phi(0) = 1, \quad \phi(\infty) = 0,$$
(23)

where the differentiation with respect to η is denoted by the prime, Gr is the mixed convection parameter, K is the porosity parameter, β is the chemical reaction parameter, Sc is the Schmidt number, $\Pr$ is the Prandtl number, Q is the heat generation parameter, Rd is the radiation parameter, We and λ denotes the Weissenberg number and curvature parameter, defined as

$$\lambda = \frac{1}{R}\sqrt{\frac{\upsilon l}{U_0}}, \quad We = \Gamma x\sqrt{\frac{U_0^3}{\upsilon l^3}}, \quad Q = \frac{lQ_0}{\rho c_p U_0}, \quad Gr = \frac{l^2 g\beta_T(T_w - T_\infty)}{U_0^2 x},$$
$$\Pr = \frac{\upsilon}{\alpha_\infty}, \quad Rd = \frac{4\sigma^* T_\infty^3}{k^*\alpha_\infty}, \quad Sc = \frac{\upsilon}{D}, \quad \beta = \frac{R^* l}{U_0}, \quad K = \frac{\upsilon l}{U_0 K^*}.$$
(24)

The physical quantity of interest skin friction coefficient $(\frac{1}{2}C_f Re_x^{1/2})$, the local Nusselt number $(NuRe_x^{-1/2})$ and Sherwood number $(ShRe_x^{-1/2})$ are defined as

$$\frac{C_f Re_x^{1/2}}{2} = f''(0) + \frac{n-1}{2}We^2[f''(0)]^3,$$
(25)

$$\frac{Nu}{Re_x^{1/2}} = -\theta'(0)\left(1 + \frac{4}{3}Rd\right),$$
(26)

$$\frac{Sh}{Re_x^{1/2}} = -\phi'(0).$$
(27)

Where $Re_x^{1/2} = x\sqrt{\frac{U_0}{\upsilon l}}$ is the local Reynold number.

2.1. Solutions by homotopy analysis technique

The governing equations of the heat transfer, Carreau fluid flows, and mass transfer along with a stretching cylinder under the effect of thermal radiation, heat generation, porous medium, free convection, and chemical reaction are solved by using the homotopy analysis method (HAM). The analytical approximation solutions are determined by initially guessing the initial solutions and the linear operators for the governing equations. Here, we take

$$f_0(\eta) = 1 - e^{-\eta}, \quad \theta_0(\eta) = e^{-\eta}, \quad \phi_0(\eta) = e^{-\eta}.$$
(28)

$$L_f = f''' + f'', \quad L_\theta = \theta'' + \theta', \quad L_\phi = \phi'' + \phi'.$$
(29)

The following properties are satisfied by the above auxiliary linear operators.

$$L_f(c_1 + c_2\eta + c_3 e^{-\eta}) = 0,$$
$$L_\theta(c_4 + c_5 e^{-\eta}) = 0,$$
$$L_\phi(c_6 + c_7 e^{-\eta}) = 0.$$
(30)

Where $c_i, i = 1, 2, \cdots, 7$ are arbitrary constants. Then, the zeroth-order deformation equations for the momentum, energy, and mass equations are formulated and we obtain

$$(1-p)L_f\{f(\eta:p) - f_0(\eta)\} = p\hbar_f N_f\{f(\eta:p), \theta(\eta:p)\},$$
(31)

$$(1-p)L_\theta\{\theta(\eta:p) - \theta_0(\eta)\} = p\hbar_\theta N_\theta\{f(\eta:p), \theta(\eta:p)\},$$
(32)

$$(1-p)L_\phi\{\phi(\eta:p) - \phi_0(\eta)\} = p\hbar_\phi N\phi\{f(\eta:p), \phi(\eta:p)\},$$
(33)

with

$$N_f\{f(\eta:p)\} = \frac{3(n-1)}{2}We^2(1+2\lambda\eta)[f''(\eta:p)]^2[\lambda f''(\eta:p) + (1+2K\eta)f'''(\eta:p)] +$$
$$(1+2\lambda\eta)f'''(\eta:p) + \frac{(n-1)}{2}We^2\lambda(1+2K\eta)[f''(\eta:p)]^3 - Kf'(\eta:p) +$$
$$2\lambda f''(\eta:p) + f(\eta:p)f''(\eta:p) - [f'(\eta:p)]^2 + Gr\theta(\eta:p),$$
(34)

$$N_\theta\{f(\eta:p), \theta(\eta:p)\} = \left[2\lambda + \Pr f(\eta:p) + 2\lambda\varepsilon\theta(\eta:p) + \frac{4}{3}\lambda Rd\right]\theta'(\eta:p) +$$
$$(1+2\lambda\eta)\left[1 + \varepsilon\theta(\eta:p) + \frac{4}{3}Rd\right]\theta''(\eta:p) +$$
$$\Pr Q\theta(\eta:p) + (1+2\lambda\eta)[\theta'(\eta:p)]^2\varepsilon,$$
.
(35)

$$N_\phi\{f(\eta:p), \phi(\eta:p)\} = [2\lambda + Scf(\eta:p)]\phi'(\eta:p) - Sc\beta\phi(\eta:p) +$$
$$(1+2\lambda\eta)\phi''(\eta:p).$$
.
(36)

The non-zero control convergence parameters for the heat equation, mass equation, and momentum equation are presented by $\hbar_\theta$, $\hbar_\phi$ and $\hbar_f$ respectively. N_f, N_ϕ and N_θ are the non-linear operators and p is the embedding parameter with the properties:

$$f(\eta:0) = f_0(\eta), \quad \theta(\eta:0) = \theta_0(\eta),$$
$$\phi(\eta:0) = \phi_0(\eta), \quad for \quad p = 0,$$
$$f(\eta:1) = f(\eta), \quad \theta(\eta:1) = \theta(\eta),$$
$$\phi(\eta:1) = \phi(\eta), \quad for \quad p = 1.$$
(37)

This implies that $f(\eta:p)$, $\theta(\eta:p)$ and $\phi(\eta:p)$ vary from initial guesses $f_0(\eta)$, $\theta_0(\eta)$ and $\phi_0(\eta)$ to the exact solutions $f(\eta)$, $\theta(\eta)$ and $\phi(\eta)$ as the embedding parameter p approach to 1 from 0. By using Taylor's series expansion, the functions $f(\eta:p)$, $\theta(\eta:p)$ and $\phi(\eta:p)$ can be expanded at $\eta = 0$ and yield

$$f(\eta:p) = f_0(\eta) + \sum_{m=1}^{\infty} f_m(\eta)p^m,$$
(38)

$$\theta(\eta:p) = \theta_0(\eta) + \sum_{m=1}^{\infty} \theta_m(\eta)p^m,$$
(39)

$$\phi(\eta:p) = \phi_0(\eta) + \sum_{m=1}^{\infty} \phi_m(\eta)p^m,$$
(40)

where

$$f_m(\eta) = \frac{1}{m!} \frac{\partial^m f(\eta:p)}{\partial p^m}\Big|_{p=0},$$

$$\theta_m(\eta) = \frac{1}{m!} \frac{\partial^m \theta(\eta:p)}{\partial p^m}\Big|_{p=0},$$

$$\phi_m(\eta) = \frac{1}{m!} \frac{\partial^m \phi(\eta:p)}{\partial p^m}\Big|_{p=0}. \tag{41}$$

Series (38)–(40) are the Maclaurin series and are assumed to be analytic in $p\epsilon[0,1]$ and converge at $p=1$ to $f(\eta)$, $\theta(\eta)$ and $\phi(\eta)$ respectively. Therefore base on the theory of HAM, the solutions of the governing equations can be written as,

$$f(\eta) = f_0(\eta) + \sum_{m=1}^{\infty} f_m(\eta),$$

$$\theta(\eta) = \theta_0(\eta) + \sum_{m=1}^{\infty} \theta_m(\eta),$$

$$\phi(\eta) = \phi_0(\eta) + \sum_{m=1}^{\infty} \phi_m(\eta). \tag{42}$$

To obtain f_m, θ_m and ϕ_m, the zeroth-order deformation Eqs. (31)–(33) are differentiated m-times with respect to p, and dividing them by $m!$ respectively. Then substituting $p=0$, and the m-th order deformation equations are determined and can be presented as

$$L_f\{f_m(\eta) - \chi_m f_{m-1}(\eta)\} = \hbar_f R^f_{m-1}\left(N_f\{f(\eta:p), \theta(\eta:p)\}\right). \tag{43}$$

$$L_\theta\{\theta_m(\eta) - \chi_m \theta_{m-1}(\eta)\} = \hbar_\theta R^\theta_{m-1}(N_\theta\{f(\eta:p), \theta(\eta:p)\}). \tag{44}$$

$$L_\phi\{\phi_m(\eta) - \chi_m \phi_{m-1}(\eta)\} = \hbar_\phi R^\phi_{m-1}\left(N_\phi\{f(\eta:p), \phi(\eta:p)\}\right). \tag{45}$$

Eqs. (43)–(45) are the so-called high-order deformation equations, and

$$\chi_m = \begin{cases} 0, & m \leqslant 1, \\ 1, & m > 1, \end{cases} \qquad R^{f,\phi,\theta}_{m-1} = \frac{1}{(m-1)!} \frac{\partial^{m-1}}{\partial p^{m-1}}\Big|_{p=0},$$

with,

$$R^f_{m-1}\left(N_f\{f(\eta:p), \theta(\eta:p)\}\right) = 2\lambda f''_{m-1} + Gr\theta_{m-1} - Kf'_{m-1} +$$

$$\frac{3(n-1)}{2} We^2(1+2\lambda\eta)\left[\sum_{i=0}^{m-1} f''_{m-1-i}\lambda\sum_{j=0}^{i} f''_{i-j}f''_i\right] +$$

$$\frac{(n-1)}{2} We^2\lambda(1+2K\eta)\left[\sum_{i=0}^{m-1} f''_{m-1-i}\lambda\sum_{j=0}^{i} f''_{i-j}f''_i\right] +$$

$$(1+2\lambda\eta)^2 \frac{3(n-1)}{2} We^2\left[\sum_{i=0}^{m-1} f''_{m-1-i}\sum_{j=0}^{i} f''_{i-j}f'''_i\right] +$$

$$(1+2\lambda\eta)f'''_{m-1} + \left[\sum_{i=0}^{m-1} f_{m-1-i}f''_i\right] - \left[\sum_{i=0}^{m-1} f_{m-1-i}f'_i\right], \tag{46}$$

$$R^\phi_{m-1}\left(N_\phi\{f(\eta:p), \phi(\eta:p)\}\right)$$

$$= (1+2\lambda\eta)\phi''_{m-1} + 2\lambda\phi'_{m-1} - Sc\beta\phi_{m-1} + Sc\left[\sum_{i=0}^{m-1} f_{m-1-i}\phi'_i\right]. \tag{48}$$

ϕ_m, θ_m and f_m for $m \geq 1$ are computed by utilizing the developed Mathematica package BVPh 2.0 by S.J.Liao [39]. The average residual error technique at mth-order approximation is applied in BVPh 2.0 to determine the optimal values for the convergence control parameters $\hbar_f$, $\hbar_\theta$ and $\hbar_\phi$ in order to guarantee the convergence of the series solutions (42). The residual error for h_f, h_θ and h_f are defined as

$$E^{Total}_m(h_f, h_\theta, h_\phi) = E^f_m(h_f) + E^\theta_m(h_\theta) + E^\phi_m(h_\phi), \tag{49}$$

where

$$E^f_m(h_f) = \frac{1}{Int+1} \sum_{i=0}^{Int} \left[N_f\left(\sum_{j=0}^{m} f_j(\eta_i)\right)\right]^2,$$

$$E^\theta_m(h_\theta) = \frac{1}{Int+1} \sum_{i=0}^{Int} \left[N_\theta\left(\sum_{j=0}^{m} \theta_j(\eta_i)\right)\right]^2,$$

$$E^\phi_m(h_\phi) = \frac{1}{Int+1} \sum_{i=0}^{Int} \left[N_\theta\left(\sum_{j=0}^{m} \phi_j(\eta_i)\right)\right]^2.$$

Where Int is an integer and $\eta_i = i(\delta\eta)$, $\delta\eta$ is the step size. The optimal values of the convergence control for h_f, h_θ and h_ϕ are calculated by the minimum of the total error $E^{Total}_m(h_f, h_\theta, h_\phi)$ at the mth-order approximation. Further information and details about the HAM can be found in the monograph by S.J.Liao "Homotopy analysis method in nonlinear differential equations" [39].

3. Results and discussions

Table 1 illustrates that the HAM series solutions converge in the interval $-0.76227 \leq h_f \leq -1.47366$ for velocity profile, $-0.32352 \leq h_\theta \leq -0.55753$ for temperature profile, and $-0.86483 \leq h_\phi \leq -0.1.30429$ for concentration profile. According to [39], any value of the so-called convergence-control parameters from these intervals can be applied to guarantee a convergent solution. The table shows the optimal convergence-control parameters for the 1st, 3rd, and 6th- order approximations respectively. However to time consumption $h_f = -1.30238$, $h_\theta = -0.47327$, and $h_\phi = -1.11716$ corresponding to the 3rd order of approximation as depicted in Table 1 are chosen for the series analytical solutions in this discussion. The total squared residual error distribution and profile of the series solution versus the order of approximations for $\lambda = 0.1$, $We = 0.2$, $Pr = 0.7$, $\varepsilon = 0.2$, $Rd = 1$, $Q = 0.2$, $n = 1.2$, $Gr = 0.2$, $Sc = 1.0$, $\beta = 0.2$, and

$$R^\theta_{m-1}(N_\theta\{f(\eta:p), \theta(\eta:p)\}) = (1+2\lambda\eta)\varepsilon\left[\sum_{i=0}^{m-1} \theta'_{m-1-i}\theta'_i\right] + (1+2\lambda\eta)\varepsilon\left[\sum_{i=0}^{m-1} \theta_{m-1-i}\theta''_i\right] +$$

$$(1+2\lambda\eta)\left(1+\frac{4}{3}Rd\right)\theta''_{m-1} + \left(2+\frac{4}{3}Rd\right)\lambda\theta'_{m-1} + \tag{47}$$

$$Q Pr\theta_{m-1} + 2\lambda\varepsilon\left[\sum_{i=0}^{m-1} \theta_{m-1-i}\theta'_i\right] + Pr\left[\sum_{i=0}^{m-1} f_{m-1-i}\theta'_i\right],$$

Table 1 Optimal value for convergence-control parameter at different mth- orders of approximation for $\lambda = 0.1$, $We = 0.2$, $Pr = 0.7$, $\varepsilon = 0.2$, $Rd = 1$, $Q = 0.2$, $n = 1.2$, $Gr = 0.2$, $Sc = 1.0$, $\beta = 0.2$, and $K = 0.2$.

m	E_m^{Total}	$\hbar_f$	$\hbar_\theta$	$\hbar_\phi$
1	3.64706×10^{-2}	-0.76227	-0.32352	-0.86483
3	1.29869×10^{-2}	-1.30238	-0.47327	-1.11716
6	7.48056×10^{-3}	-1.47366	-0.55753	-1.30429

Table 2 Square residual errors at different mth-orders of the series solutions for $\lambda = 0.1$, $We = 0.2$, $Pr = 0.7$, $\varepsilon = 0.2$, $Rd = 1$, $Q = 0.2$, $n = 1.2$, $Gr = 0.2$, $Sc = 1.0$, $\beta = 0.2$, and $K = 0.2$.

m	E_m^f	E_m^θ	E_m^ϕ	E_m^{Total}	CPU time (s)
10	4.01177×10^{-5}	6.02106×10^{-3}	2.31196×10^{-6}	6.06349×10^{-3}	140.263
20	2.78659×10^{-5}	4.24332×10^{-3}	9.65423×10^{-7}	4.27215×10^{-3}	3153.24
30	2.27167×10^{-5}	3.52493×10^{-3}	5.53648×10^{-7}	3.54820×10^{-3}	18325.3
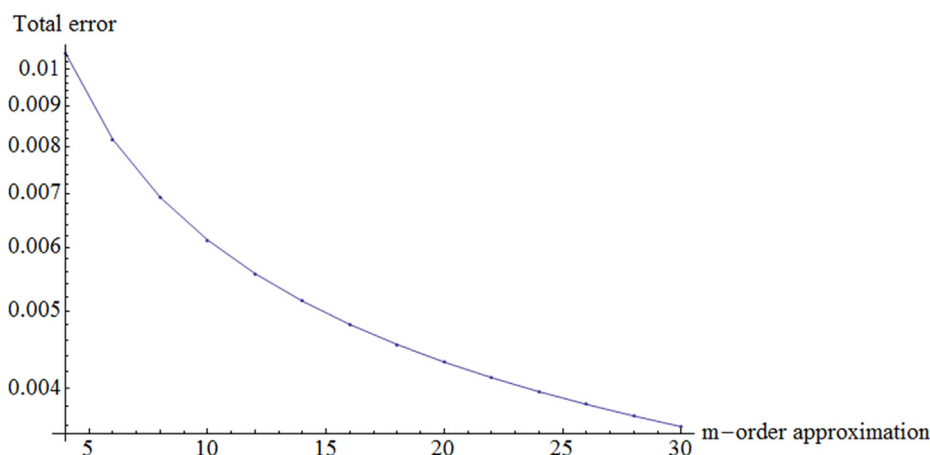
Fig. 2 Total error profile for $\lambda = 0.1$, $We = 0.2$, $Pr = 0.7$, $\varepsilon = 0.2$, $Rd = 1$, $Q = 0.2$, $n = 1.2$, $Gr = 0.2$, $Sc = 1.0$, $\beta = 0.2$, and $K = 0.2$ and the convergence-control parameters $\hbar_f = -1.30238$, $\hbar_\theta = -0.47327$ and $\hbar_\phi = -1.11716$.

Table 3 Comparison of the local skin friction coefficient for different values of curvature parameter λ when $K = Gr = We = 0$ and $n = 1$.

λ	[28]	[27]	[4]	Present
0.0	-1.000000	-1.000000	–	-1.000000
0.3	-1.111165	-1.111150	-1.111138	-1.118788
0.5	-1.188727	-1.188695	–	-1.195933
0.7	-1.257045	-1.257020	-1.257011	-1.271896

$K = 0.2$ are displayed in Table 2 and Fig. 2 respectively. As seen in the figure and table that increasing the order of approximation reduces, the total residual error. For convenience, the 20th order of HAM series solutions is taken for computing the remaining results.

Table 3 compares the skin friction coefficient $f''(0)$ under certain limiting cases for different values of λ with respect to some previous reports in the literature to validate the computed series solution. As indicated in the table, the present results are in close agreement with the findings of [28,27],

Table 4 Comparison of the local Nusselt number, $-\theta'(0)$ for different values of Pr with $\lambda = We = \varepsilon = Rd = Q = 0$ and $n = 1$.

Pr	[4]	[5]	[41]	Present
1	0.5820	0.5822	0.5820	0.5835
10	2.3080	2.3062	2.3080	2.3095
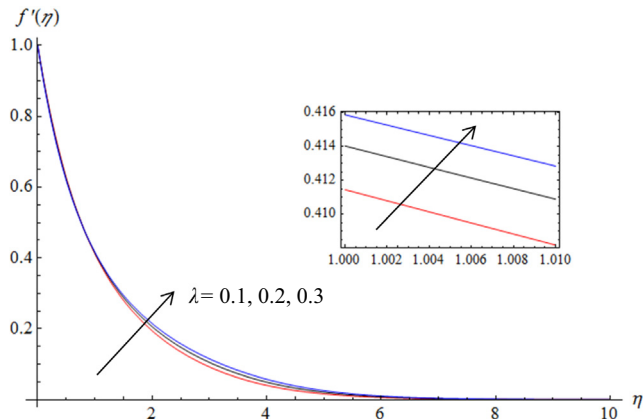
Fig. 3 Velocity profile of $f'(\eta)$ versus η for various values of λ with $Gr = 0.2$, $K = 0.2$, $n = 1.2$ and $We = 0.2$.
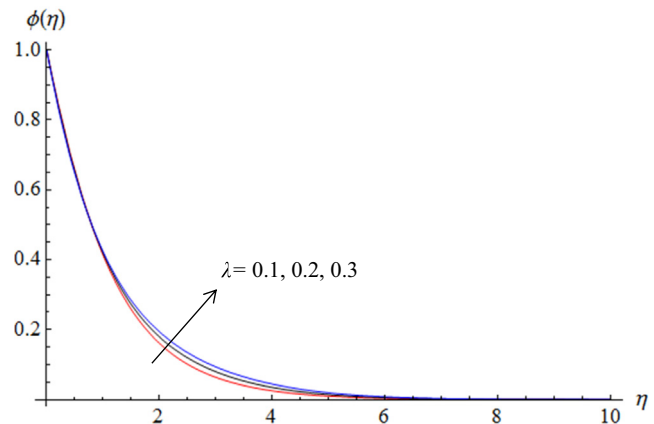
Fig. 4 Temperature profile of $\theta(\eta)$ versus η for various values of λ with $Gr = 0.2$, $K = 0.2$, $n = 1.2$, $We = 0.2$, $Pr = 0.7$, $Rd = 1$, $Q = 0.2$ and $\varepsilon = 0.2$.

Fig. 5 Concentration profile of $\phi(\eta)$ versus η for various values of λ with $Gr = 0.2$, $K = 0.2$, $n = 1.2$, $We = 0.2$, $Pr = 0.7$, $Rd = 1$, $Q = 0.2$, $Sc = 1.0$, $\beta = 0.2$, and $\varepsilon = 0.2$.
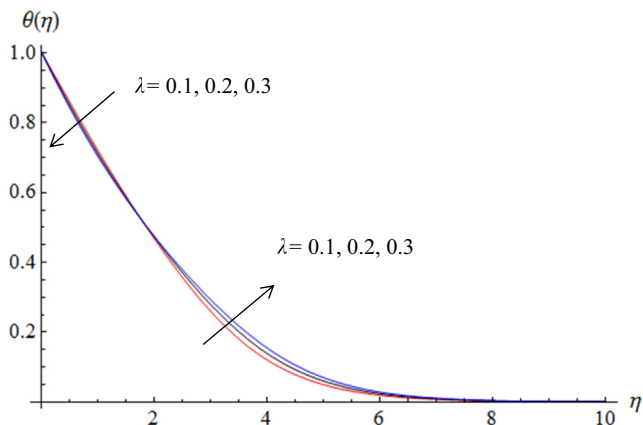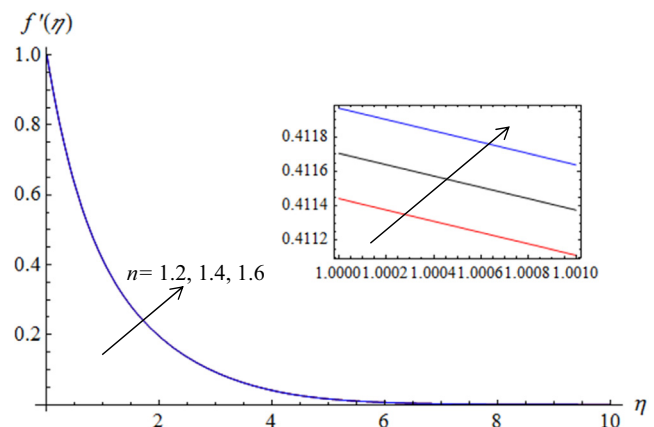
Fig. 6 Velocity profile of $f'(\eta)$ versus η for various values of n with $Gr = 0.2$, $K = 0.2$, $\lambda = 0.1$, $We = 0.2$, $Pr = 0.7$, $Rd = 1$, $Q = 0.2$ and $\varepsilon = 0.2$.

and [4] respectively. Table 4 illustrates the comparison of the local Nusselt number $-\theta'(0)$ at $\lambda = We = \varepsilon = Rd = Q = 0$ and $n = 1$ for various values of Pr with the results in [4], [5] and [41] respectively. Again, the solutions of the present research are in good agreement with the existing outputs. This gives the assurance for computing and analyzing the remaining tasks of the present study. For the following discussion, the calculation for the influence of the pertinent parameters are obatained for $\lambda = 0.1, 0.2, 0.3$, $Pr = 0.7, 1, 2$, $\varepsilon = 0.0, 0.2, 0.4$, $K = 0, 0.2, 0.4$, $Gr = 0, 0.2, 0.4$, $\beta = 0.0, 0.2, 0.4$, $We = 0.2, 0.4, 0.6$, $Q = 0.2, 0.4, 0.6$, $n = 0.5, 1.2, 1.4, 1.6$, $Sc = 1, 1.5, 2.0$, and $Rd = 1, 2, 3$.

The influence of the curvature parameter λ, on the velocity profile is presented in Fig. 3. A smaller value of the curvature parameter λ indicates that the cylinder has a larger radius. Thus, the contact area of the fluid with the boundary is less for a greater curvature parameter λ. Consequently, the surface resistive force that acts on the fluid is reduced. Therefore, an increment in the velocity is observed in Fig. 3 when the value of the curvature parameter λ is increased. Besides, the concentration profile is also an increasing function of the curvature parameter λ as depicted in Fig. 5. Furthermore, less contact surface allows less heat transfer from the cylinder to the ambient fluid, and accordingly, the temperature near the surface of the cylinder declines as the curvature parameter λ increases (see Fig. 4). The temperature far away from the cylinder is reduced when λ is diminished as revealed in Fig. 4.

Figs. 6-8 demonstrate the relationship between the power-law index n and the distribution of the velocity, temperature, and concentration respectively. The momentum boundary layer thickness rises with the power-law index. Therefore, the velocity of the fluid is improved as displayed in Fig. 6. Notably, the fluid will become a Newtonian fluid as n approaches 1, which leads to a larger viscosity for the fluid and hence a drop in velocity. The temperature and concentration profiles show growth when the value of the power-law index n is reduced (see Figs. 7 and 8). An inverse behavior of the velocity profiles against the Weissenberg number We is observed in Figs. 9 and 10. Fig. 9 shows the shear-thinning fluid, $n < 1$ has greater velocity distribution with decreasing Weissenberg number We. However, in the shear-thickening fluid, $n > 1$ there is an improvement in the velocity profile when the value of Weissenberg number We is increased as depicted in Fig. 10. Physically, We is a linear function of the relaxation time and we have assumed $\Gamma\dot{\gamma} < 1$. Thus, high viscosity is produced in the shear-thinning fluid and low viscosity in the shear-
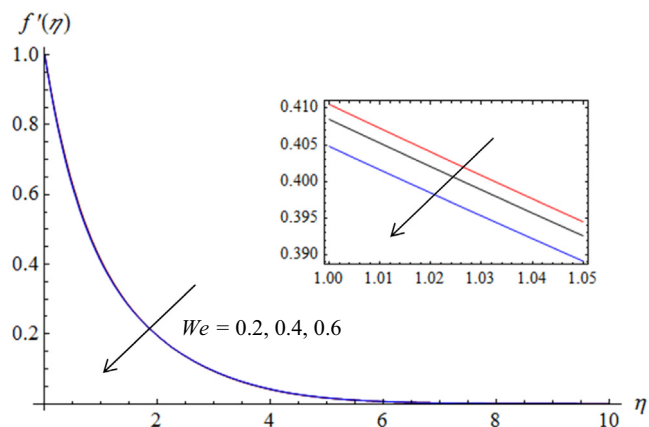
Fig. 9 Velocity profile of $f'(\eta)$ versus η for various values of We with $Gr = 0.2$, $K = 0.2$, $\lambda = 0.1$, $n = 0.5$, $Pr = 0.7$, $Rd = 1$, $Q = 0.2$ and $\varepsilon = 0.2$.
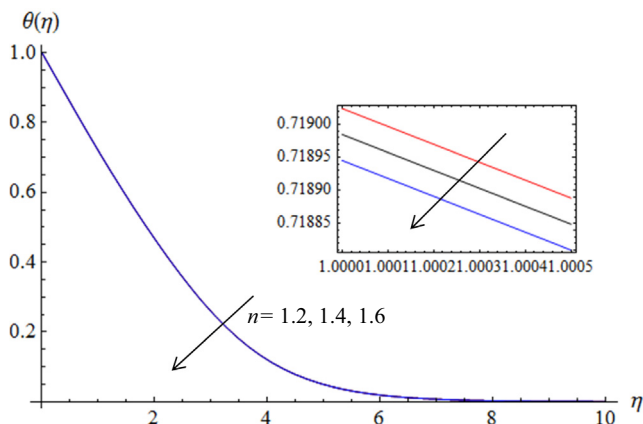
Fig. 7 Temperature profile of $\theta(\eta)$ versus η for various values of n with $Gr = 0.2$, $K = 0.2$, $\lambda = 0.1$, $We = 0.2$, $Pr = 0.7$, $Rd = 1$, $Q = 0.2$ and $\varepsilon = 0.2$.
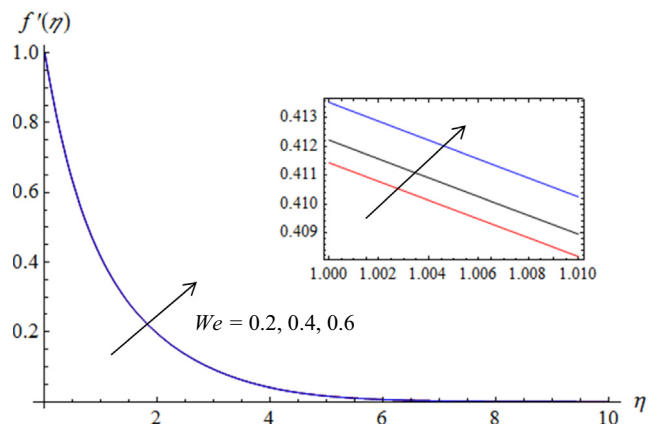
Fig. 10 Velocity profile of $f'(\eta)$ versus η for various values of We with $Gr = 0.2$, $K = 0.2$, $\lambda = 0.1$, $n = 1.2$, $Pr = 0.7$, $Rd = 1$, $Q = 0.2$ and $\varepsilon = 0.2$.
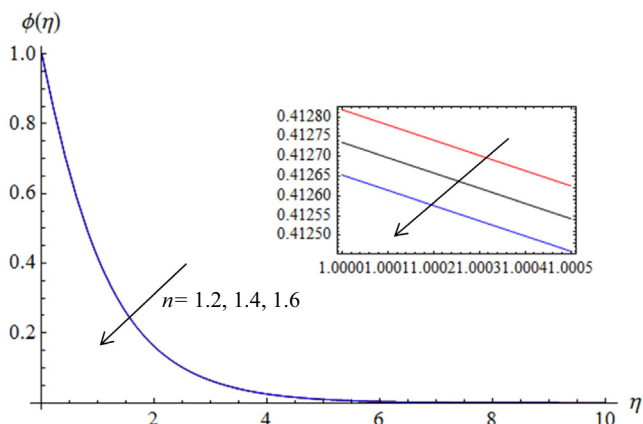
Fig. 8 Concentration profile of $\phi(\eta)$ versus η for various values of λ with $Gr = 0.2$, $K = 0.2$, $\lambda = 0.1$, $We = 0.2$, $Pr = 0.7$, $Rd = 1$, $Q = 0.2$, $Sc = 1.0$, $\beta = 0.2$, and $\varepsilon = 0.2$.
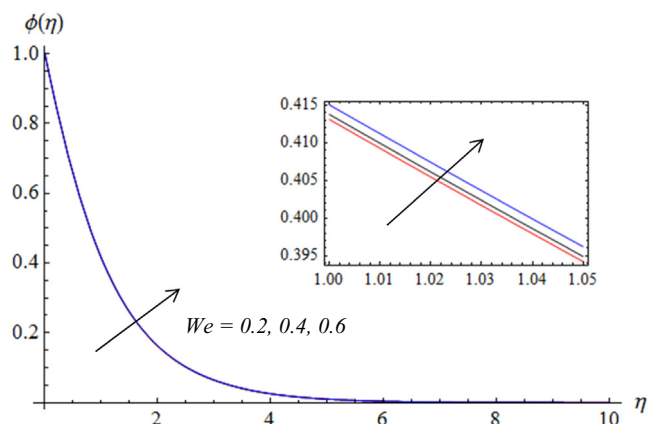
Fig. 11 Concentration profile of $\phi(\eta)$ versus η for various values of We with $Gr = 0.2$, $K = 0.2$, $\lambda = 0.1$, $n = 0.5$, $Pr = 0.7$, $Rd = 1$, $Q = 0.2$, $Sc = 1.0$, $\beta = 0.2$, and $\varepsilon = 0.2$.
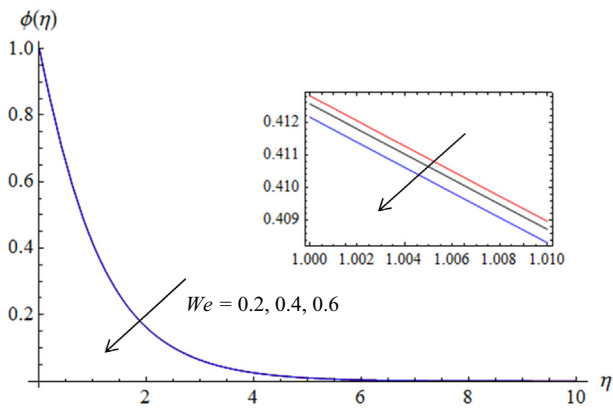
Fig. 12 Concentration profile of $\phi(\eta)$ versus η for various values of We with $Gr = 0.2$, $K = 0.2$, $\lambda = 0.1$, $n = 1.2$, $Pr = 0.7$, $Rd = 1$, $Q = 0.2$, $Sc = 1.0$, $\beta = 0.2$, and $\varepsilon = 0.2$.
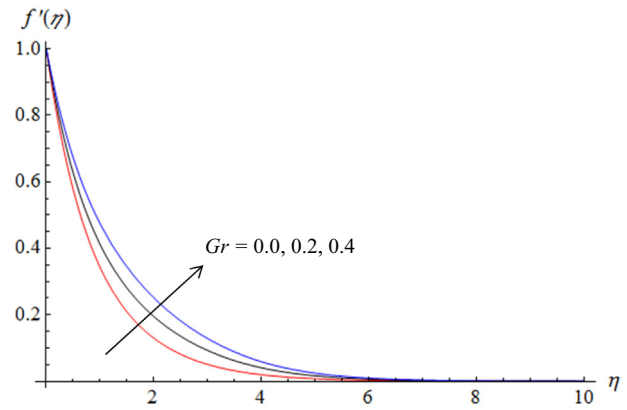
Fig. 15 Velocity profile of $f'(\eta)$ versus η for various values of Gr with $We = 0.2$, $K = 0.2$, $\lambda = 0.1$, $n = 1.2$, $Pr = 0.7$, $Rd = 1$, $Q = 0.2$ and $\varepsilon = 0.2$.
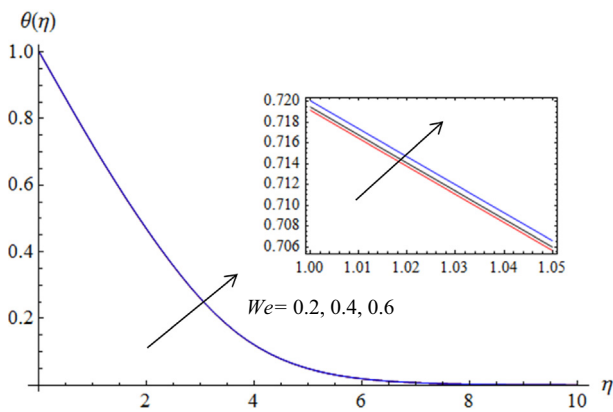
Fig. 13 Temperature profile of $\theta(\eta)$ versus η for various values of We with $Gr = 0.2$, $K = 0.2$, $\lambda = 0.1$, $n = 0.5$, $Pr = 0.7$, $Rd = 1$, $Q = 0.2$ and $\varepsilon = 0.2$.
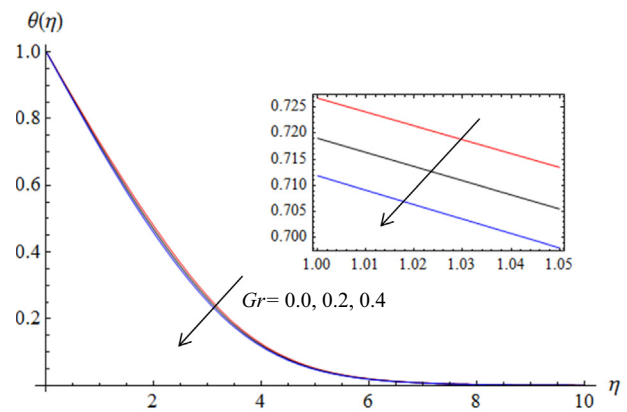
Fig. 16 Temperature profile of $\theta(\eta)$ versus η for various values of Gr with $We = 0.2$, $K = 0.2$, $\lambda = 0.1$, $n = 1.2$, $Pr = 0.7$, $Rd = 1$, $Q = 0.2$ and $\varepsilon = 0.2$.
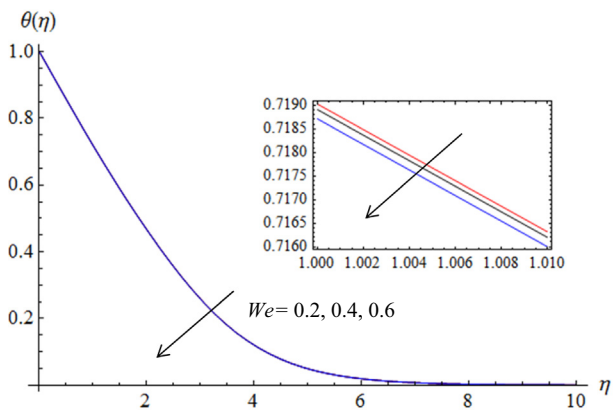
Fig. 14 Temperature profile of $\theta(\eta)$ versus η for various values of We with $Gr = 0.2$, $K = 0.2$, $\lambda = 0.1$, $n = 1.2$, $Pr = 0.7$, $Rd = 1$, $Q = 0.2$ and $\varepsilon = 0.2$.
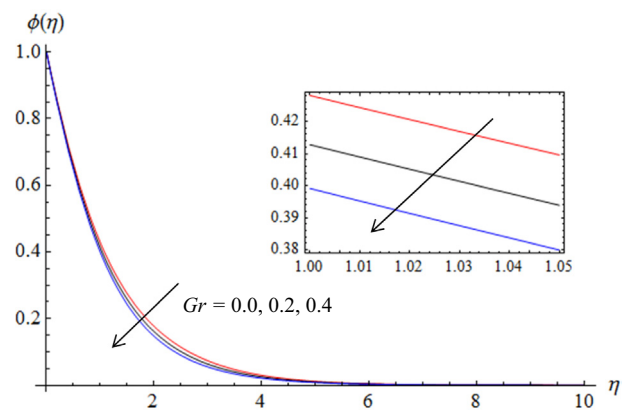
Fig. 17 Concentration profile of $\phi(\eta)$ versus η for various values of Gr with $We = 0.2$, $K = 0.2$, $\lambda = 0.1$, $n = 1.2$, $Pr = 0.7$, $Rd = 1$, $Q = 0.2$, $Sc = 1.0$, $\beta = 0.2$, and $\varepsilon = 0.2$.

thickening fluid when the shear rate diminishes. In contrast, the fluid concentration for $n < 1$ increases for a bigger value of the Weissenberg number We (see Fig. 11). However, a reverse trend is noticed for shear-thickening fluid as depicted in Fig. 12. A similar phenomenon is realized for the fluid temperature as indicated in Figs. 13 and 14 respectively.

An increase in the magnitude of Gr designates an augmentation in the temperature difference $T_w - T_\infty$, which has enhanced the buoyancy forces and thus increased the pressure gradient in the fluid. As a result, the flow of the Carreau fluid is accelerated as shown in Fig. 15. The enhancement of the natural convection has increased the velocity and the thickness of the momentum layer. Variation of temperature and concentration for several values of the Gr numbers are plotted in Figs. 16 and 17 respectively. As seen, the temperature and concentration decrease with increment in the Gr. The thickness of the thermal or concentration boundary layer is reduced. Fig. 18 demonstrates the effects of the permeability parameter K on the velocity distribution. The velocity is found to decrease with the increase of K. Physically, the presence of a porous medium
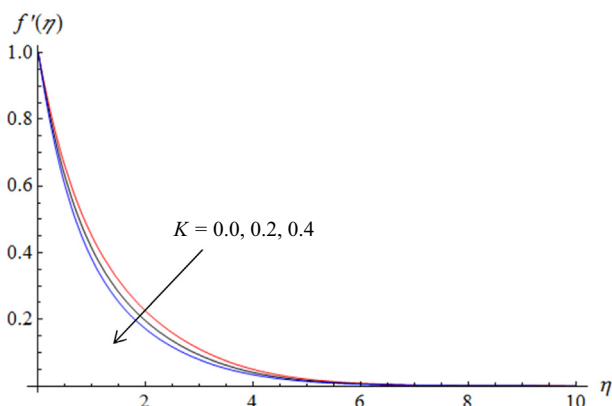
Fig. 20 Concentration profile of $\phi(\eta)$ versus η for various values of K with $We = 0.2$, $Gr = 0.2$, $\lambda = 0.1$, $n = 1.2$, $Pr = 0.7$, $Rd = 1$, $Q = 0.2$, $Sc = 1.0$, $\beta = 0.2$, and $\varepsilon = 0.2$.
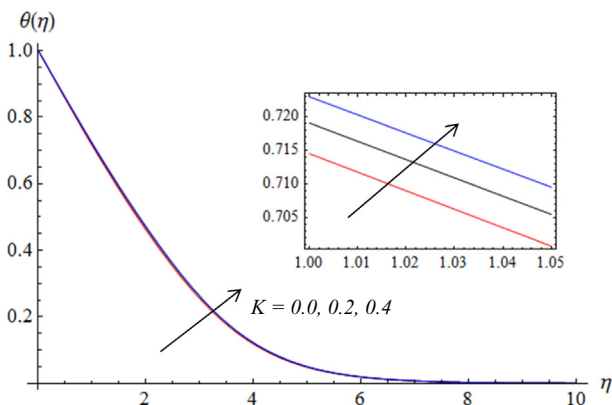
Fig. 18 Velocity profile of $f'(\eta)$ versus η for various values of K with $We = 0.2$, $Gr = 0.2$, $\lambda = 0.1$, $n = 1.2$, $Pr = 0.7$, $Rd = 1$, $Q = 0.2$ and $\varepsilon = 0.2$.

Fig. 21 Concentration profile of $\phi(\eta)$ versus η for various values of Sc with $We = 0.2$, $Gr = 0.2$, $\lambda = 0.1$, $n = 1.2$, $Pr = 0.7$, $Rd = 1$, $Q = 0.2$, $K = 0.2$, $\beta = 0.2$, and $\varepsilon = 0.2$.

Fig. 19 Temperature profile of $\theta(\eta)$ versus η for various values of K with $We = 0.2$, $Gr = 0.2$, $\lambda = 0.1$, $n = 1.2$, $Pr = 0.7$, $Rd = 1$, $Q = 0.2$ and $\varepsilon = 0.2$.
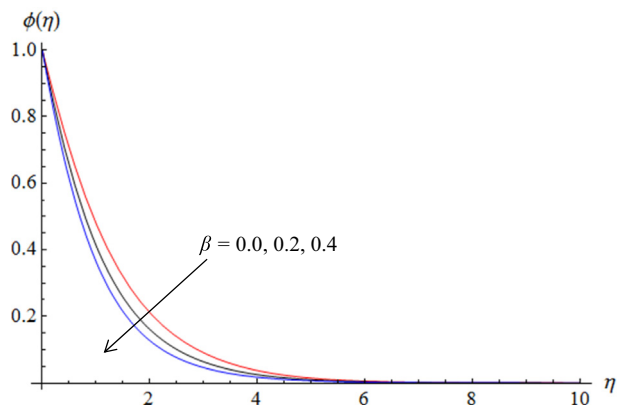
Fig. 22 Concentration profile of $\phi(\eta)$ versus η for various values of β with $We = 0.2$, $Gr = 0.2$, $\lambda = 0.1$, $n = 1.2$, $Pr = 0.7$, $Rd = 1$, $Q = 0.2$, $K = 0.2$, $Sc = 1.0$, and $\varepsilon = 0.2$.

has improved the medium resistance to the fluid flow. The decreasing of the fluid velocity has induced an escalation in the temperature and concentration profiles. This can be explored in Figs. 19 and 20 respectively.
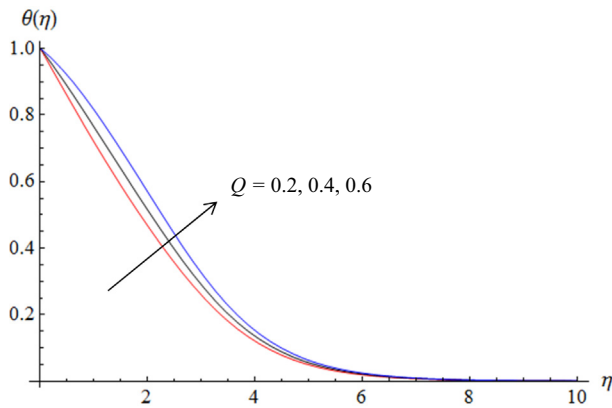
Fig. 23 Temperature profile of $\theta(\eta)$ versus η for various values of Q with $We = 0.2$, $Gr = 0.2$, $\lambda = 0.1$, $n = 1.2$, $Pr = 0.7$, $Rd = 1$, $K = 0.2$ and $\varepsilon = 0.2$.
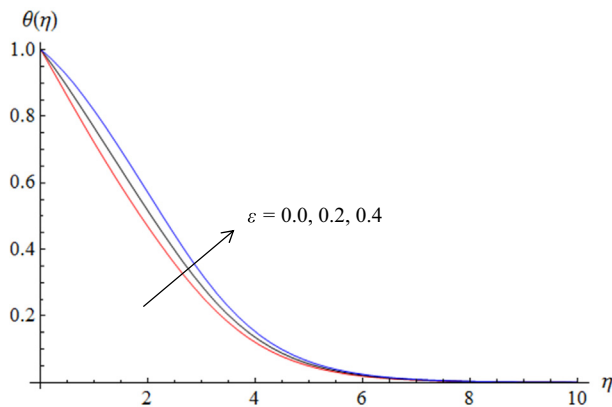
Fig. 24 Temperature profile of $\theta(\eta)$ versus η for various values of ε with $We = 0.2$, $Gr = 0.2$, $\lambda = 0.1$, $n = 1.2$, $Pr = 0.7$, $Rd = 1$, $K = 0.2$ and $Q = 0.2$.
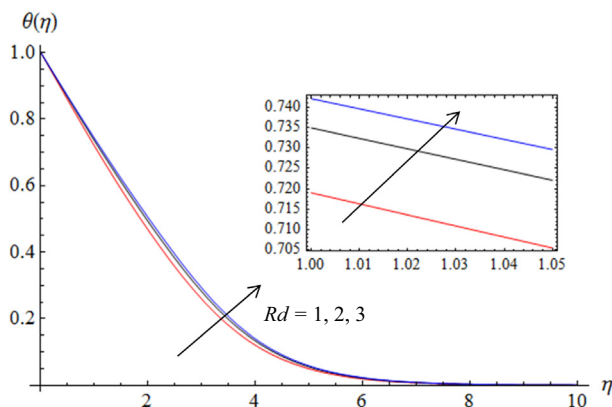
The effect of the Schmidt number and chemical reaction parameter on the concentration distribution can be determined from Figs. 21 and 22 respectively. In Fig. 21, it is observed that the concentration decreases with an increase in Sc and thus initiated a reduction in the concentration boundary layer thickness. Schmidt number is defined as the ratio of momentum diffusivity and mass diffusivity. An increment of Sc indicates an enchantment of the rate of viscous diffusion or a decrement of the rate of mass diffusion. Similarly, the concentration in the fluid is reduced as the rate of the chemical reaction is increased. This is exhibited in Fig. 22. This happens because more chemically reactive species are consumed for the larger value of the chemical reaction parameter.

Fig. 23 interprets the influence of the heat generation parameter Q on the temperature profile. The thermal boundary layer is improved for incremented values of the Q. A similar phenomenon is observed in Fig. 25 for the response of the temperature to the radiation parameters Rd. The temperature increases with increasing magnitude of Rd. This finding is in agreement with the fact that heat generation and thermal radiation when heat is added to the flow system [42]. To facilitate the cooling process, for example, in a cooling reactor system, the impact of the heat source and thermal radiation should be maintained at its minimum or optimal level. More kinetic energy is supplied to the fluid since more energy is transferred from the cylinder to the fluid as the thermal conductivity parameter ε is increased. The increment of the thermal conductivity has induced an improvement in temperature distribution as established in Fig. 24. A large value of Prandtl number Pr indicates a slow heat diffusion since Pr is defined as rates of momentum diffusivity to thermal diffusivity. Hence, the thermal boundary layer thickness is reduced when the number of Pr is raised as shown in Fig. 26.

The behavior of local skin friction, local Nusselt number, and local Sherwood number for various values of relevant variables λ, We, K, Gr, Pr, β, ε, Rd, Q, Sc, and n are presented in Tables 5–7 respectively. Here, we observe that the local skin friction is lower when a larger value of parameters We at $n = 0.5$ is applied. A reverse behavior is detected for parameters We at $n = 1.2$. Increasing the power-law index n, curvature parameter λ, Prandtl number Pr, and the porous parameter K has improved the local skin friction respectively

Fig. 25 Temperature profile of $\theta(\eta)$ versus η for various values of Rd with $We = 0.2$, $Gr = 0.2$, $\lambda = 0.1$, $n = 1.2$, $Pr = 0.7$, $\varepsilon = 0.2$, $K = 0.2$ and $Q = 0.2$.
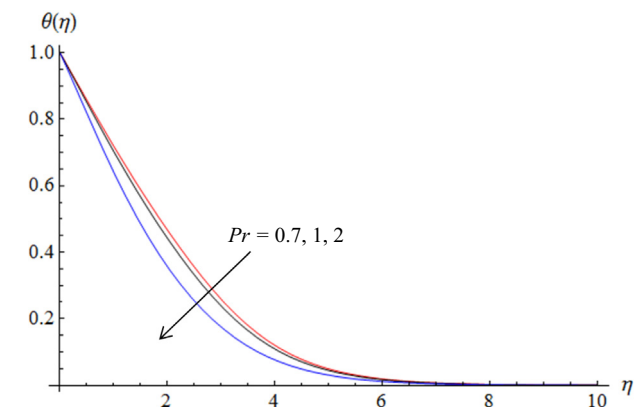
Fig. 26 Temperature profile of $\theta(\eta)$ versus η for various values of Pr with $We = 0.2$, $Gr = 0.2$, $\lambda = 0.1$, $n = 1.2$, $Rd = 1$, $\varepsilon = 0.2$, $K = 0.2$ and $Q = 0.2$.

Table 5 Local skin friction for different values of embedding parameters.

We	n	λ	Gr	K	Pr	Rd	Q	ε	$C_f Re_x^{1/2}$
0.2	0.5	0.1	0.2	0.2	0.7	1	0.2	0.2	−0.987622
0.4	–	–	–	–	–	–	–	–	−0.978099
0.6	–	–	–	–	–	–	–	–	−0.960565
0.2	1.2	–	–	–	–	–	–	–	−0.991864
0.4	–	–	–	–	–	–	–	–	−0.995403
0.6	–	–	–	–	–	–	–	–	−1.001100
0.2	1.4	–	–	–	–	–	–	–	−0.993053
–	1.6	–	–	–	–	–	–	–	−0.994233
–	1.2	0.2	–	–	–	–	–	–	−1.03252
–	–	0.3	–	–	–	–	–	–	−1.072600
–	–	0.1	0.0	–	–	–	–	–	−1.138710
–	–	–	0.4	–	–	–	–	–	−0.852891
–	–	–	0.2	0.0	–	–	–	–	−0.888204
–	–	–	–	0.4	–	–	–	–	−1.087330
–	–	–	–	0.2	1	–	–	–	−0.994554
–	–	–	–	–	2	–	–	–	−1.00438
–	–	–	–	–	0.7	2	–	–	−0.988997
–	–	–	–	–	–	3	–	–	−0.987648
–	–	–	–	–	–	1	0.4	–	−0.985412
–	–	–	–	–	–	–	0.6	–	−0.978123
–	–	–	–	–	–	–	0.2	0.4	−0.991308
–	–	–	–	–	–	–	–	0.6	−0.990789

Table 6 Local Nusselt number for different values of embedding parameters.

Rd	Pr	ε	Q	λ	We	n	K	Gr	$Nu/Re_x^{1/2}$
1	0.7	0.2	0.2	0.1	0.2	1.2	0.2	0.2	−0.659064
2	–	–	–	–	–	–	–	–	−0.986748
3	–	–	–	–	–	–	–	–	−1.316900
1	1	–	–	–	–	–	–	–	−0.686278
–	2	–	–	–	–	–	–	–	−0.811897
–	0.7	0.4	–	–	–	–	–	–	−0.643692
–	–	0.6	–	–	–	–	–	–	−0.630266
–	–	0.2	0.4	–	–	–	–	–	−0.485520
–	–	–	0.6	–	–	–	–	–	−0.292999
–	–	–	0.2	0.2	–	–	–	–	−0.728095
–	–	–	–	0.3	–	–	–	–	−0.792806
–	–	–	–	0.1	0.4	1.2	–	–	−0.659388
–	–	–	–	–	0.6	–	–	–	−0.659927
–	–	–	–	–	0.2	1.4	–	–	−0.659171
–	–	–	–	–	–	1.6	–	–	−0.659281
–	–	–	–	–	–	1.2	0.0	–	−0.671169
–	–	–	–	–	–	–	0.4	–	−0.648690
–	–	–	–	–	–	–	0.2	0.0	−0.638605
–	–	–	–	–	–	–	–	0.4	−0.678204
–	–	–	–	–	–	0.5	–	0.2	−0.658679
–	–	–	–	–	0.4	–	–	–	−0.657809
–	–	–	–	–	0.6	–	–	–	−0.656161

as shown in Table 5. On the other hand, the $\left| f''(0) \right|$ is reduced by the increasing values of Gr, β, ε, Rd, and Q. Further, the local Nusselt number $\left| \theta'(0) \right|$ shows a decrement for a larger

value of K, ε, Q, and We at n = 0.5. A slight increase happens for the local Nusselt number when n = 1.2 for a greater value of the number of We. The rate of heat transfer is enhanced when the n, Pr, Gr, Rd and λ increase. Higher values of λ,

Table 7 Local Sherwood number for different values of embedding parameters.

β	Sc	λ	We	n	K	Gr	$Sh/Re_x^{1/2}$
0.2	1.0	0.1	0.2	1.2	0.2	0.2	−0.795346
0.0	–	–	–	–	–	–	−0.639331
0.4	–	–	–	–	–	–	−0.924422
0.2	1.5	–	–	–	–	–	−0.991592
–	2.0	–	–	–	–	–	−1.161195
–	1.0	0.2	–	–	–	–	−0.836502
–	–	0.3	–	–	–	–	−0.876936
–	–	0.1	0.4	–	–	–	−0.795717
–	–	–	0.6	–	–	–	−0.796324
–	–	–	0.2	1.4	–	–	−0.795471
–	–	–	–	1.6	–	–	−0.795594
–	–	–	–	1.2	0.0	–	−0.807191
–	–	–	–	–	0.4	–	−0.784910
–	–	–	–	–	0.2	0.0	−0.774681
–	–	–	–	–	–	0.4	−0.813924
–	–	–	–	0.5	–	0.2	−0.794903
–	–	–	0.4	–	–	–	−0.793892
–	–	–	0.6	–	–	–	−0.791958

Gr, Sc, and We at $n = 1.2$ raise the value of the local Sherwood number $\left| \phi'(0) \right|$. In contrast, the Sherwood number is reduced for increasing values of β, K, and We at $n = 0.5$.

4. Conclusion

The analysis of the heat and mass transfer of the natural convection Carreau fluid flow through a vertical stretching cylinder in a porous medium under the influence of the chemical reaction has been constructed and discussed. The Carreau fluid is a combination of power-law and Newtonian fluid model and it is significant in chemical engineering and polymeric suspensions. The characteristic of pharmaceutical chemicals, paints, polymer fluids, Polyvinyl Chloride, and Polyethylene can be described by the Carreau fluid model. Moreover, the effect of the variable thermal conductivity, heat generation, and thermal radiation is also considered. These effects play a vital role in optimizing the heat transfer process especially in cooling devices, wire coating, copper thinning, water heater and thermoelastic dampling. The derived highly nonlinear partial differential equations are solved by using the homotopy analysis method. The obtained analytical approximation solutions are validated by comparing the results of a limiting case with the solutions determined in the published literature. The effects of the variation of the embedded parameters on the velocity, temperature, and concentration profiles are presented. From the findings, we can conclude:

- Rd, Q, K, and ε have enhanced the temperature distribution when being increased. In contrast, the growth of Gr, n, and Pr have reduced the temperature. The temperature distribution is increased when We increases at $n = 0.5$ but is decreased at $= 1.2$.

- The temperature near the cylinder surface is increased by the curvature parameter λ but the parameter has reduced the temperature at a region far away from the cylinder.
- The velocity profile is improved with the increasing λ, Gr, and n, whereas the declining of K makes the fluid move faster. Interestingly, the magnitude of the velocity shows a conflicting behavior when We is amplified at $n = 0.5$ and $n = 1.2$ respectively. The velocity decreases when $n = 0.5$ but increases when $= 1.2$.
- The concentration in the fluid shows an improvement when either Gr, or n is reduced. Furthermore, the concentration profiles have been boosted by increasing λ, We, Sc, K, and β. The concentration profile is improved as We increases at $n = 0.5$ but decreases at $n = 1.2$.
- The rate of heat transfer decreases with K, ε, Q, and We at $n = 0.5$ and increases with n, Pr, Gr, Rd, λ and We at $n = 1.2$.
- Raising values of λ, Gr, Sc, and We at $n = 1.2$ raised the rate of concentration diffusion. In contrast, increasing values of β, K, and We at $n = 0.5$ have reduced the rate.
- The local skin friction coefficient increases with We at $n = 1.2$, n, λ, Pr, and K. However, the local skin friction coefficient is reduced by Gr, β, ε, Rd, and Q.

The present study has considered the non-slip boundary condition only. To be more realistic, the analysis should be extended to include the slip condition [12]. Furthermore, the effects of convective boundary condition [43], nonlinear thermal radiation [34], homogeneous-heterogeneous reactions [17], nonlinear stretching rate [44] and magnetic fields [26] can be considered in future. Besides, the effects that have been concerned in the present study can be included in a different type of fluid model such as tangent hyperbolic [45], Maxwell [46], and Williamson [9] to examine their impact. Finally, for further investigations, one can deliberate the fluid flow over

an inclined stretching cylinder or a nonlinear stretching cylinder with suction [43].

References

[1] K. Vajravelu, K.V. Prasad, S.R. Santhi, Axisymmetric magneto-hydrodynamic (MHD) flow and heat transfer at a non-isothermal stretching cylinder, Appl. Math. Comput. 219 (8) (2012) 3993–4005.

[2] S. Mukhopadhyay, A. Ishak, Mixed convection flow along a stretching cylinder in a thermally stratified medium, J. Appl. Math. 2012 (2012) 1–8.

[3] E. Elbashbeshy, T. Emam, M. El-Azab, K. Abdelgaber, Effect of magnetic field on flow and heat transfer over a stretching horizontal cylinder in the presence of a heat source/sink with suction/injection, Journal of Applied, Mech. Eng. 1 (2012) 1–5.

[4] V. Poply, P. Singh, K. Chaudhary, Analysis of laminar boundary layer flow along a stretching cylinder in the presence of thermal radiation, WSEAS Trans Fluid Mech. 8 (2013) 159–164.

[5] E. Elbashbeshy, T. Emam, M. El-Azab, K. Abdelgaber, Laminar boundary layer flow along a stretching cylinder embedded in a porous medium, Int. J. Phys. Sci. 7 (2012) 3067–3072.

[6] S. Mukhopadhyay, Mixed convection boundary layer flow along a stretching cylinder in porous medium, J. Petrol. Sci. Eng. 96-97 (2012) 73–78.

[7] A.K. Pandey, M. Kumar, Natural convection and thermal radiation influence on nanofluid flow over a stretching cylinder in a porous medium with viscous dissipation, Alexandria Eng. J. 56 (1) (2017) 55–62.

[8] W. Jamshed, S. Uma Devi S, M. Goodarzi, M. Prakash, K. Sooppy Nisar, M. Zakarya, A.-H. Abdel-Aty, Evaluating the unsteady casson nanofluid over a stretching sheet with solar thermal radiation: An optimal case study, Case Studies, Therm. Eng. 26 (2021) 101160, https://doi.org/10.1016/j.csite.2021.101160.

[9] S. Jain, A. Parmar, Radiation effect on MHD williamson fluid flow over stretching cylinder through porous medium with heat source, Applications of Fluid Dynamics. Springer (2018) 61–78.

[10] T. Hayat, S. Asad, A. Alsaedi, Flow of variable thermal conductivity fluid due to inclined stretching cylinder with viscous dissipation and thermal radiation, Appl. Math. Mech. 35 (6) (2014) 717–728.

[11] T. Salahuddin, M.Y. Malik, A. Hussain, S. Bilal, M. Awais, Combined effects of variable thermal conductivity and MHD flow on pseudoplastic fluid over a stretching cylinder by using Keller box method, Inf. Sci. Lett. 5 (1) (2016) 11–19.

[12] M.K. Murthy, C.S. Raju, V. Nagendramma, S. Shehzad, A.J. Chamkha: Magnetohydrodynamics boundary layer slip Casson fluid flow over a dissipated stretched cylinder, in: Defect and Diffusion Forum: 2019. Trans Tech Publ: 73-82.

[13] M. Malik, M. Bibi, F. Khan, T. Salahuddin, Numerical solution of Williamson fluid flow past a stretching cylinder and heat transfer with variable thermal conductivity and heat generation/absorption, AIP Adv. 6 (2016) 035101.

[14] M. Tamoor, M. Waqas, M.I. Khan, A. Alsaedi, T. Hayat, Magnetohydrodynamic flow of Casson fluid over a stretching cylinder, Results Phys. 7 (2017) 498–502.

[15] N. Najib, N. Bachok, N.M. Arifin, A. Ishak, Stagnation point flow and mass transfer with chemical reaction past a stretching/shrinking cylinder, Sci. Rep. 4 (2014) 1–7.

[16] T. Hayat, M. Anwar, M. Farooq, A. Alsaedi, MHD stagnation point flow of second grade fluid over a stretching cylinder with heat and mass transfer, International Journal of Nonlinear Sciences and Numerical, Simulation. 15 (2014) 365–376.

[17] M. Malik, T. Salahuddin, A. Hussain, S. Bilal, M. Awais, Homogeneous-heterogeneous reactions in Williamson fluid model over a stretching cylinder by using Keller box method, AIP Adv. 5 (2015) 107227.

[18] F. Mabood, I. Tlili, A. Shafiq, Features of inclined magnetohydrodynamics on a second-grade fluid impinging on vertical stretching cylinder with suction and Newtonian heating, Math. Methods Appl. Sci. (2020).

[19] T. Walelign, E. Haile, T. Kebede, A. Walelgn, Analytical study of heat and mass transfer in MHD flow of chemically reactive and thermally radiative Casson nanofluid over an inclined stretching cylinder, J. Phys. Commun. 4 (2020) 125003.

[20] P.J. Carreau, Rheological equations from molecular network theories, Trans. Soc. Rheol. 16 (1) (1972) 99–127.

[21] I. Khan, Shafquatullah, M.Y. Malik, A. Hussain, M. Khan, Magnetohydrodynamics Carreau nanofluid flow over an inclined convective heated stretching cylinder with Joule heating, Results Phys. 7 (2017) 4001–4012.

[22] M. Khan, M. Azam, A.S. Alshomrani, On unsteady heat and mass transfer in Carreau nanofluid flow over expanding or contracting cylinder with convective surface conditions, J. Mol. Liq. 231 (2017) 474–484.

[23] M. Azam, M. Khan, A.S. Alshomrani, Unsteady radiative stagnation point flow of MHD Carreau nanofluid over expanding/contracting cylinder, Int. J. Mech. Sci. 130 (2017) 64–73.

[24] T. Salahuddin, A. Hussain, M. Malik, M. Awais, M. Khan, Carreau nanofluid impinging over a stretching cylinder with generalized slip effects: Using finite difference scheme, Results Phys. 7 (2017) 3090–3099.

[25] I. Khan, S. Ullah, M.Y. Malik, A. Hussain, Numerical analysis of MHD Carreau fluid flow over a stretching cylinder with homogenous-heterogeneous reactions, Results Phys. 9 (2018) 1141–1147.

[26] D. Gopal, S.H.S. Naik, N. Kishan, C. Raju, The impact of thermal stratification and heat generation/absorption on MHD carreau nano fluid flow over a permeable cylinder, SN Appl. Sci. 2 (2020) 1–10.

[27] K. Gangadhar, K. Ramana, O.D. Makinde, B.R. Kumar, MHD flow of a Carreau fluid past a stretching cylinder with Cattaneo-Christov heat flux using spectral relaxation method, in: Defect and Diffusion Forum: 2018. Trans Tech Publ: 91-105.

[28] M. Khan, A.S. Alshomrani, Characteristics of melting heat transfer during flow of Carreau fluid induced by a stretching cylinder, The, Eur. Phys. J. E. 40 (2017) 1–9.

[29] T. Salahuddin, Carreau fluid model towards a stretching cylinder: Using Keller box and shooting method, Ain Shams Eng. J. 11 (2) (2020) 495–500.

[30] M. Khan, Hashim, M. Hussain, M. Azam, Magnetohydrodynamic flow of Carreau fluid over a convectively heated surface in the presence of non-linear radiation, J. Magn. Magn. Mater. 412 (2016) 63–68.

[31] M. Khan, M. Azam, A.S. Alshomrani, Effects of melting and heat generation/absorption on unsteady Falkner-Skan flow of Carreau nanofluid over a wedge, Int. J. Heat Mass Transf. 110 (2017) 437–446.

[32] M. Waqas, M.I. Khan, T. Hayat, A. Alsaedi, Numerical simulation for magneto Carreau nanofluid model with thermal radiation: a revised model, Comput. Methods Appl. Mech. Eng. 324 (2017) 640–653.

[33] T. Hayat, I. Ullah, B. Ahmad, A. Alsaedi, Radiative flow of Carreau liquid in presence of Newtonian heating and chemical reaction, Results Phys. 7 (2017) 715–722.

[34] D. Lu, M. Ramzan, N. Ul Huda, J.D. Chung, U. Farooq, Nonlinear radiation effect on MHD Carreau nanofluid flow over a radially stretching surface with zero mass flux at the surface, Sci. Rep. 8 (2018) 1–17.

[35] W. Jamshed, Numerical investigation of MHD impact on Maxwell nanofluid, Int. Commun. Heat Mass Transfer 120 (2021) 104973.

[36] A. Shafiq, Z. Hammouch, A. Turab, Impact of radiation in a stagnation point flow of Walters' B fluid towards a Riga plate, Thermal Sci. Eng. Progress 6 (2018) 27–33.

[37] A. Shafiq, Z. Hammouch, H.F. Oztop: Radiative MHD flow of third-grade fluid towards a stretched cylinder, in: International Conference on Computational Mathematics and Engineering Sciences: 2019. Springer: 166-185.

[38] S. Liao, Notes on the homotopy analysis method: some definitions and theorems, Commun. Nonlinear Sci. Numer. Simul. 14 (4) (2009) 983–997.

[39] S. Liao (Ed.), Homotopy Analysis Method in Nonlinear Differential Equations, Springer Berlin Heidelberg, Berlin, Heidelberg, 2012.

[40] S. Liao, Advances in the homotopy analysis method, World Scientific, 2013.

[41] A. Ishak, R. Nazar, Laminar boundary layer flow along a stretching cylinder, Eur. J. Sci. Res. 36 (2009) 22–29.

[42] W. Jamshed, K.S. Nisar, R.W. Ibrahim, T. Mukhtar, V. Vijayakumar, F. Ahmad, Computational frame work of Cattaneo-Christov heat flux effects on Engine Oil based Williamson hybrid nanofluids: A thermal case study, Case Studies Thermal Eng. 26 (2021) 101179, https://doi.org/10.1016/j.csite.2021.101179.

[43] G. Rasool, A. Shafiq, Numerical exploration of the features of thermally enhanced chemically reactive radiative Powell-Eyring nanofluid flow via Darcy medium over non-linearly stretching surface affected by a transverse magnetic field and convective boundary conditions, Appl. Nanosci. (2020) 1–18.

[44] W. Jamshed, A. Aziz, Cattaneo-Christov based study of TiO2–CuO/EG Casson hybrid nanofluid flow over a stretching surface with entropy generation, Appl. Nanosci. 8 (2018) 685–698.

[45] W. Jamshed, K.S. Nisar, R.W. Ibrahim, F. Shahzad, M.R. Eid, Thermal expansion optimization in solar aircraft using tangent hyperbolic hybrid nanofluid: a solar thermal application, J. Mater. Res. Technol. 14 (2021) 985–1006.

[46] Anum Shafiq, Chaudry Masood Khalique, Lie group analysis of upper convected Maxwell fluid flow along stretching surface, Alexandria Eng. J. 59 (4) (2020) 2533–2541.